Modification of relaxation dynamics in $Tb^{3+}:Y_3Al_5O_{12}$ nanopowders

Thomas Lutz,[1,*] Lucile Veissier,[1,†] Philip J. T. Woodburn,[2] Rufus L. Cone,[2] Paul E. Barclay,[1]
Wolfgang Tittel,[1,‡] and Charles W. Thiel[2]
[1] *Institute for Quantum Science and Technology and Department of Physics & Astronomy,*
University of Calgary, Calgary, Alberta T2N 1N4, Canada
[2] *Department of Physics, Montana State University, Bozeman, Montana 59717, USA*

(Received 6 November 2017; revised manuscript received 13 July 2018; published 29 August 2018)

Nanostructured rare-earth-ion-doped materials are increasingly being investigated for on-chip implementations of quantum information processing protocols as well as commercial applications such as fluorescent lighting. However, achieving high-quality and optimized materials at the nanoscale is still challenging. Here we present a detailed study into the restriction of phonon processes in the transition from bulk crystals to small (⩽40-nm) nanocrystals by observing the relaxation dynamics between crystal-field levels of $Tb^{3+}:Y_3Al_5O_{12}$. We find that the population relaxation dynamics are modified as the particle size is reduced, consistent with our simulations of inhibited relaxation through a modified vibrational density of states and hence modified phonon emission. However, our experiments also indicate that nonradiative processes not driven by phonons are also present in the smaller particles, causing transitions and rapid thermalization between the levels on a time scale of <100 ns.

DOI: 10.1103/PhysRevB.98.054308

I. INTRODUCTION

Crystalline materials doped with impurities, such as rare-earth ions or diamond silicon-vacancy and nitrogen-vacancy centers, have found many applications in fields as diverse as quantum information processing [1–4], quantum memories [5–7], sensing [8], lasers [9], and phosphors [10,11]. Nanometer-sized structures fabricated from these materials have begun to be investigated for on-chip implementations of these applications. In addition, small nanophosphors are desired for high-quality window materials used in lamps as well as for state-of-the-art displays [12,13]. Finally, nanopowders have also been proposed for optical refrigeration applications where their modified phonon spectrum and particle morphology could enhance the cooling efficiency [14].

Nanomaterials can be obtained through different routes: nanostructures can be milled or etched from high-quality bulk materials, and nanocrystals can be obtained through chemical synthesis, mechanical crushing, or ablation techniques. The transition to nanosized structures generally introduces detrimental effects such as poor crystal quality, surface effects, and amorphous behavior that can severely restrict practical applications [15,16]. While some of these effects, such as the increasing surface-to-volume ratio, are fundamental, others can be minimized by optimizing the fabrication process [15]. Indeed, in some cases, both chemical synthesis and fabrication methods starting with bulk materials produced high-quality materials [17,18]. However, none of these structures have allowed study of the effects of decreasing dimensions on phonon-mediated population dynamics. Furthermore, a general procedure for achieving consistently high-quality nanomaterials is still unknown and many open questions remain regarding the transition to smaller sizes, requiring further systematic studies.

During the transition from a bulk material to nanostructures, many material properties change. One interesting effect is the predicted modification of the vibrational density of states (VDOS) in small structures. Whereas a bulk crystal has a Debye VDOS (a continuous function that increases with the square of the vibrational frequency), the distribution becomes discrete in small crystallites, exhibiting gaps and even a cutoff below which no phonons are supported. Furthermore, phononic crystals—nanomachined, periodic structures—can feature engineered frequency band gaps where vibrations are forbidden [19]. These approaches to phonon engineering could potentially benefit applications in the field of quantum information, in particular, quantum memories, since the absence of phonons could enhance spin-population lifetimes as well as optical coherence times. Modifications of population dynamics in rare-earth-ion-doped nanocrystals have been previously reported by Meltzer *et al.* [20,21], Liu *et al.* [22], and Mercier *et al.* [23], and it was suggested that the changes were due to phonon suppression in the nanocrystals. However, the particles employed in some of those studies were not sufficiently small to suppress phonons at the desired frequencies, and locally elevated temperatures caused by the optical excitation of the powder materials might explain some of the observed effects. Thus, unambiguous confirmation of the suppression of phonon-mediated relaxation in optical centers through VDOS engineering remains an open challenge.

In this paper we examine the effect of the transition from bulk crystals to ⩽40-nm particles (see Fig. 1) on the population dynamics between excited-state crystal-field levels in

---

[*] Current address: ETH Zürich, Zürich, Switzerland.

[†] Current address: Laboratoire Aimé Cotton, CNRS-UPR 3321, Université Paris-Sud, Orsay Cedex, France.

[‡] Current address: QuTech and Faculty of Electrical Engineering, Mathematics and Computer Science, Delft Technical University, Delft, The Netherlands.

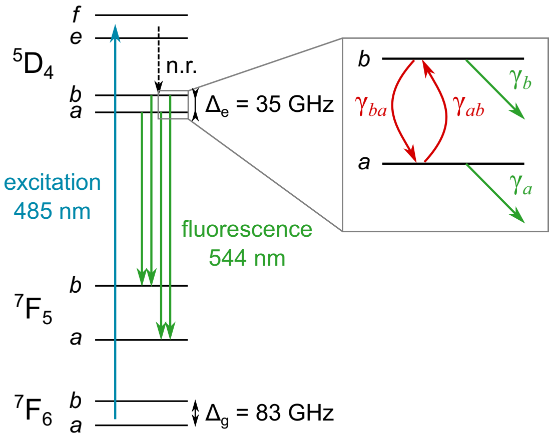

FIG. 1. Relevant energy levels of Tb^{3+}:Y$_3$Al$_5$O$_{12}$(vertical axis not to scale) for measurement of the population relaxation between the first two crystal-field levels within the ^{5}D$_4$ excited-state manifold. A pulsed laser excited the ions from the ^{7}F$_6$ a ground state to the ^{5}D$_4$ f excited state, from where they decay rapidly into ^{5}D$_4$ a and b. The resulting fluorescence due to the four ^{5}D$_4$ $a/b \rightarrow ^7$ F$_5$ a/b transitions was collected, spectrally resolved, and then analyzed. Inset: Relaxation processes (nonradiative, red; radiative, green) for populations on the two excited levels ^{5}D$_4$ a/b (see definitions in the text).

Tb^{3+}-doped Y$_3$Al$_5$O$_{12}$ (YAG). Specifically, we study the influence of size restriction on the relaxation dynamics and equilibrium population distribution between the crystal-field levels, i.e., thermalization. We observe that the population dynamics are strongly modified for smaller particles, which can be explained by a modified density of states. However, we also find that the thermal population distribution exhibited by the nanopowders is the same as in the bulk material. As described in detail in later sections, the observation of rapid thermalization suggests that, in addition to possible phonon suppression, other nonphononic processes—e.g., related to surface defects or energy transfer [24]—are introduced, enabling rapid thermalization of populations between the closely spaced energy levels.

II. EXPERIMENTAL DETAILS

We chose Tb^{3+}-doped Y$_3$Al$_5$O$_{12}$ (YAG) since the combination of its energy level structure and its high acoustic velocity is well suited to investigation of the effects of size on the direct phonon process. More precisely, the small excited-state splitting $\Delta_e = 35$ GHz (denoted Δ in the following) between the Tb^{3+} crystal-field levels ^{5}D$_4$ a/b (see Fig. 1), together with the acoustic velocity of 6400 m/s [25], results in an expected suppression of the direct phonon process for relatively large particles, ~100 nm in diameter. In addition, in the bulk crystal, the inhomogeneous broadening of about 20 GHz allows one to selectively address each of the ^{5}D$_4$ a/b crystal-field levels. Furthermore, the ground-state splitting $\Delta_g = 83$ GHz is large enough that resonant phonons are not expected to be inhibited in the >40-nm-diameter nanocrystals, and we could therefore directly measure the internal sample temperature through the ratio of population in the two levels ^{7}F$_6$ a/b.

We created our powders using a sol-gel synthesis (method 1 [26]) and a modified sol-gel synthesis with a freeze-drying step under vacuum and at temperatures below −20 °C to restrict agglomeration (method 2 [27]). Each method leads to slightly different particle morphologies and size distributions. Additional size control can be achieved by changing the annealing duration and temperature. In this way we were able to vary the nanocrystal diameter d between 40 and 500 nm and between 40 and 70 nm using methods 1 and 2, respectively. We evaluated the crystal quality of our powders using a scanning electron microscope (SEM), a transmission electron microscope (TEM), x-ray diffraction (XRD), and optical spectroscopy methods (Appendixes A and B). From these measurements we conclude that the bulk crystal quality can be maintained for crystallites with diameters down to ~80 nm. For smaller sizes, we observe a slight decrease in crystal quality that manifests itself in an increase in the inhomogeneous broadening. Measurements of the radiative lifetime as a function of the particle size (Appendix A) confirm that we can approximately treat the powders as individual particles rather than large agglomerates, with method 2 producing less agglomeration than method 1.

All powders were mounted in an unsealed glass cuvette within an Oxford Instruments cryostat. The samples were held at temperatures from ~1 up to 10 K; for temperatures below 2.17 K, the samples were immersed in superfluid liquid helium, whereas for higher temperatures, the samples were cooled with a continuous flow of helium vapor. A pulsed Hänsch-style nitrogen-laser-pumped dye laser [28] with peak powers of up to 10 kW, a pulse duration of 6 ns, and a repetition rate of 6 Hz was used with Coumarin 481 dye to provide excitation light at 485 nm. As shown in Fig. 1, we resonantly excited Tb ions from the ground state ^{7}F$_6$ a to the ^{5}D$_4$ f level, a transition that provides strong absorption. From the ^{5}D$_4$ f level, the population rapidly decays in less than 1 ns nonradiatively by emission of high-frequency acoustic phonons into the two levels ^{5}D$_4$ a and b. Using a SPEX 1401 monochromator (<3-GHz resolution), we selectively collected fluorescence from each of the four ^{5}D$_4$ $a/b \rightarrow ^7$ F$_5$ a/b transitions. The collection was at an angle of 90° relative to the excitation laser, and the fluorescence was measured using a photomultiplier tube (Hamamatsu R928) terminated with a variable resistance that allowed for time resolutions as fast as 100 ns.

For all powders and experimental configurations described below, we directly measured the local temperature through the relative population in the two levels ^{7}F$_6$ a and b, as detailed in Appendix C. We find no local heating, thus confirming that observed changes in relaxation dynamics were not due to elevated sample temperatures.

III. TIME-RESOLVED FLUORESCENCE MEASUREMENTS

Before studying the population dynamics of the ^{5}D$_4$ a/b levels, we ensured that we could selectively collect fluorescence from the two excited levels ^{5}D$_4$ a/b for each of our samples. We recorded fluorescence spectra by scanning the monochromator over the four lines connecting ^{5}D$_4$ $a/b \rightarrow ^7$ F$_5$ a/b, with typical fluorescence spectra shown in Fig. 2. We observed that the smallest nanocrystals feature an increased inhomogeneous broadening compared to the bulk (for details see

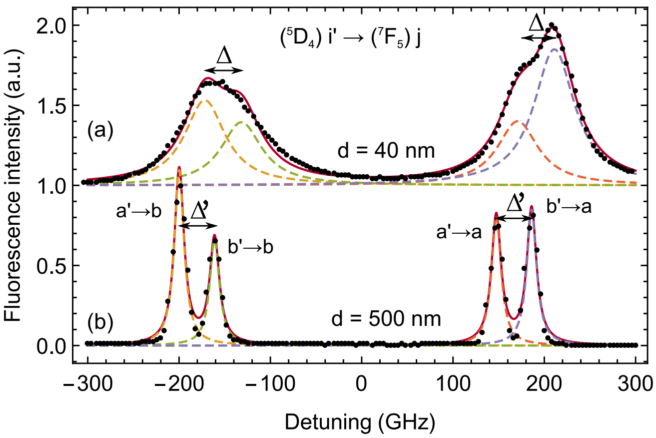

FIG. 2. Fluorescence spectra at 5 K of (a) a 40-nm-diameter powder and (b) a 500-nm-diameter powder (synthesized via method 1). Each spectrum (black circles) was fitted by the sum of four identical Lorentzian lines with the same pairwise energy splitting Δ (Δ′). For $d = 40$ nm the width is 53 GHz and Δ is 40 GHz, and for $d = 500$ nm the width is 13 GHz and Δ′ is 39 GHz.

Appendix B). As a consequence, some fraction of the detected emission originates from the neighboring transition. Since this can lead to observations that could wrongfully be interpreted as modifications in relaxation dynamics, it must be considered in the analysis of any obtained data as described later.

Following this initial characterization, we recorded fluorescence decays from the two crystal-field levels $^5\mathrm{D}_4\, a/b$ at a temperature of 1.5 K. The individual decays were collected by sequentially tuning the monochromator on resonance with each of the four transitions $^5\mathrm{D}_4\;\; a/b \rightarrow {}^7\mathrm{F}_5\, a/b$. The specific frequencies of these transitions were obtained from the fluorescence spectra measured for each sample as described above. After excitation of the $^5\mathrm{D}_4\; f$ level, 2 THz above $^5\mathrm{D}_4\, a$, the population decays rapidly first into both $^5\mathrm{D}_4\, a/b$ levels and from there into $^7\mathrm{F}_5\, a/b$. In a sufficiently large crystal, fluorescence decays originating from the four transitions (see Fig. 3) are composed of two components. The first component corresponds to the nonradiative decay of population from $^5\mathrm{D}_4\, b$ to $^5\mathrm{D}_4\, a$ and manifests itself in the fluorescence decays from $^5\mathrm{D}_4\, a$ to $^7\mathrm{F}_5\, a/b$ as a fill-in, i.e., an increase in the fluorescence intensity with time, and in the fluorescence from $^5\mathrm{D}_4\, b$ to $^7\mathrm{F}_5\, a/b$ as an initial, fast decay, both with the same characteristic time of about 0.2 ms. The second, long component corresponds to the radiative decay, with a characteristic time of about 4 ms.

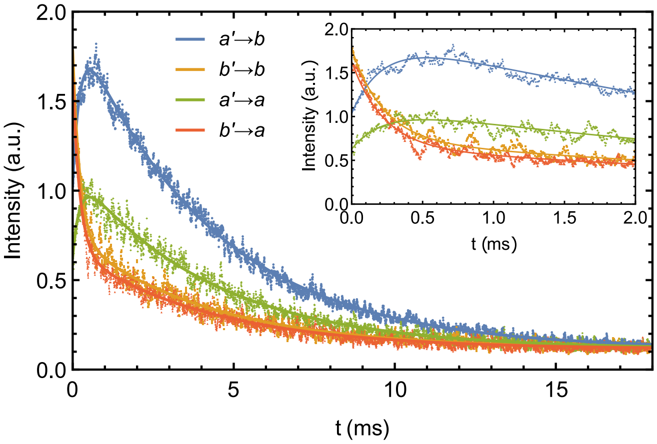

FIG. 3. Fluorescence decays $^5\mathrm{D}_4\, a/b \;\rightarrow\; {}^7\mathrm{F}_5\, a/b$ at 1.5 K in large crystallites ($d = 500$ nm). The experimental points were fitted by Eq. (9) (solid lines), resulting in $\gamma_a = 237 \pm 0.5$ Hz and $\gamma_{ba} = 3.36 \pm 0.03$ kHz. Inset: Magnification of the first 2 ms of the decay.

The dynamics are captured by the rate equations

$$\dot{n}_a^{\mathrm{bulk}}(t) = -(\gamma_a + \gamma_{ab})n_a^{\mathrm{bulk}}(t) + \gamma_{ba}\, n_b^{\mathrm{bulk}}(t),$$
$$\dot{n}_b^{\mathrm{bulk}}(t) = +\gamma_{ab}\, n_a^{\mathrm{bulk}}(t) - (\gamma_b + \gamma_{ba})n_b^{\mathrm{bulk}}(t), \tag{1}$$

where $n_{a/b}^{\mathrm{bulk}}(t)$ denote the populations in the levels $^5\mathrm{D}_4\, a/b$ at a time t after excitation (see inset in Fig. 1). The rates $\gamma_{a/b}$ correspond to the radiative decay from each level into the $^7\mathrm{F}_5$ multiplet, and we assume that $\gamma_a = \gamma_b$. The latter assumption is justified by the good quality of our fits. The rates $\gamma_{ab/ba}$ characterize the nonradiative processes coupling the levels $^5\mathrm{D}_4\, a$ and b (absorption/emission of a phonon with energy $\hbar\Delta$). At high temperatures, they are equal, but γ_{ab} depends on the number of phonons available. Therefore, they differ at low temperatures; in fact, we can write

$$\gamma_{ab} = e^{-\hbar\Delta/kT}\gamma_{ba}, \tag{2}$$

where $\hbar\Delta$ is the energy difference between the a and the b levels, k the Boltzmann constant, and T the temperature. Note that relaxation into the ground-state multiplet $^7\mathrm{F}_6$ is ignored [experimentally and in Eq. (1), due to the transitions' comparably low rates]. The solutions of Eq. (1) are

$$n_a^{\mathrm{bulk}}(t,T) = \frac{1}{1+e^{-\hbar\Delta/kT}}[(n_{a0}\, e^{-\hbar\Delta/kT} - n_{b0})$$
$$\times\, e^{-[\gamma_a+\gamma_{ba}(1+e^{-\hbar\Delta/kT})]t} + (n_{a0}+n_{b0})e^{-\gamma_a t}],$$
$$n_b^{\mathrm{bulk}}(t,T) = \frac{1}{1+e^{-\hbar\Delta/kT}}[-(n_{a0}\, e^{-\hbar\Delta/kT} - n_{b0})$$
$$\times\, e^{-[\gamma_a+\gamma_{ba}(1+e^{-\hbar\Delta/kT})]t} + (n_{a0}+n_{b0})$$
$$\times\, e^{-\hbar\Delta/kT} e^{-\gamma_a t}], \tag{3}$$

where n_{a0} and n_{b0} are the initial populations in the $^5\mathrm{D}_4\, a/b$ levels.

The fluorescence that we measured is proportional to the populations but must be weighted by the transition strengths, which manifest themselves in the corresponding fluorescence spectrum. The spectra (see Fig. 2) can be modeled by four Lorentzian functions with amplitude $d_{i\rightarrow j}$, center frequency $f_{0,i\rightarrow j}$ (separated by Δ for the a and b transitions), and width γ:

$$I_{i\rightarrow j}(f) = \frac{d_{i\rightarrow j}}{1+\left(\frac{f-f_{0,i\rightarrow j}}{\gamma}\right)^2}. \tag{4}$$

Therefore, the fluorescence intensity detected at frequency f is

$$i_{\mathrm{bulk}}(t,T,f) = \sum_{j=a,b} I_{a\rightarrow j}(f)\, n_a^{\mathrm{bulk}}(t,T)$$
$$+ \sum_{j=a,b} I_{b\rightarrow j}(f)\, n_b^{\mathrm{bulk}}(t,T). \tag{5}$$

The parameters $d_{i\to j}$, $f_{0,i\to j}$, Δ, and γ were obtained for each powder by fitting the fluorescence spectra. Then we could fit all four florescence decays at once by taking the above expression at the frequencies we picked for the measurements (f_{aa}, f_{ba}, f_{ab}, f_{bb}). This enabled us to obtain one set of parameters for each powder sample, and at the same this takes into to account fluorescence that originates from neighboring transitions. The only free parameters were the rates γ_a and γ_{ba}, as well as parameters accounting for experimental imperfections: a background fluorescence and four independent scaling factors for the four fluorescence intensities (i.e., we allowed the collection efficiency to vary). The initial population n_{a0} ($n_{b0} = 1 - n_{a0}$) was let free for the large samples ($d > 100$ ns); the fit gave values around 0.5. This is in agreement with random relaxation from $^5\mathrm{D}_4\ f$ via many paths to $^5\mathrm{D}_4\ a/b$. Therefore, we fixed $n_{a0} = n_{b0} = 0.5$ for the small samples where the fits tended to give larger uncertainties. The fit reproduced the experimental data very well and resulted in $\gamma_a = 237 \pm 0.5$ Hz and $\gamma_{ba} = 3.36 \pm 0.03$ kHz for the largest powder sample ($d = 500$ nm) (see Fig. 3).

By reducing the size of the particles, we expect to introduce a frequency cutoff in the VDOS below which phonons are not allowed. Consequently, we expect to observe a change in the nonradiative relaxation between the two closely spaced crystal-field levels $^5\mathrm{D}_4\ a$ and b, represented by the terms with the rate γ_{ba} in Eq. (3). The cutoff frequency is given by

$$\nu_{\min} = \eta \frac{c}{\pi d}, \tag{6}$$

where c is the sound velocity, d is the diameter of the crystal, and η is a numerical constant that equals 2.05 for one spherical particle and phonon modes with negligible broadening [29]. According to this formula, YAG particles (where $c = 6400$ m/s [25]) with diameters below $d_0 = 100$ nm should not be able to support phonons at $\Delta = 35$ GHz, corresponding to the splitting between the two crystal-field levels $^5\mathrm{D}_4\ a/b$.

If the phonons are completely forbidden, the population decays simply become

$$\begin{aligned} n_a^{\mathrm{np}}(t) &= n_{a0}\, e^{-\gamma_a t}, \\ n_b^{\mathrm{np}}(t) &= n_{b0}\, e^{-\gamma_a t}, \end{aligned} \tag{7}$$

with $n_{a/b}^{np}$ the population in the levels $^5\mathrm{D}_4\ a/b$ for the case where phonons are not allowed. Here, the first, fast component completely disappeared, and the populations are independent of the temperature. If we assume $n_{a0} = n_{b0} = 0.5$, we can write the fluorescence intensity as

$$i_{\mathrm{np}}(t, f) = \sum_{i,j} I_{i\to j}(f)\, e^{-\gamma_a t}. \tag{8}$$

Because our powder samples inevitably exhibit some distribution of particle sizes (the horizontal error bars in Fig. 4 correspond to one standard deviation in the respective size distribution), the nonradiative relaxation should be suppressed in more and more particles as the mean of the size distribution is reduced below ~100 nm. This should lead to a gradual decrease in the amplitude of the fast component of the fluorescence decays. For a distribution of particle sizes, the fluorescence intensity can be written as

$$i_{\mathrm{tot}}(t, T, f) = (1 - \beta)\, i_{\mathrm{bulk}}(t, T, f) + \beta\, i_{\mathrm{np}}(t, f), \tag{9}$$

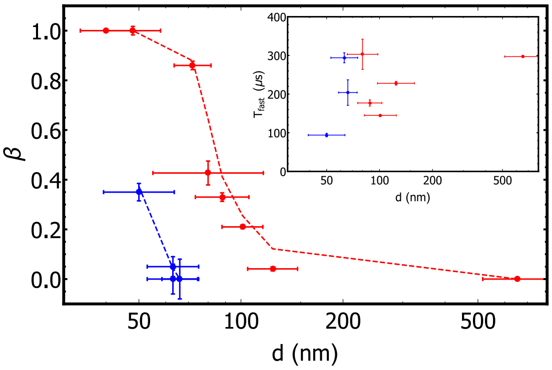

FIG. 4. Fraction of particles suppressing phonons β obtained from an average of the fits of Eq. (9) to the four decays $^5\mathrm{D}_4\, a, b \to {}^7\mathrm{F}_5\, a, b$ as a function of the average nanocrystal diameter d for powder 1 (red) and powder 2 (blue) at 1.5 K. Simulations are depicted using dashed lines. Inset: Characteristic time of the fast decay component as a function of the nanocrystal diameter d.

where β is the fraction of particles for which we get a cutoff of the VDOS at Δ. Therefore we fitted the experimental decays by Eq. (9) and obtained the parameter β for each sample. As shown in Fig. 4, we find that for particles created using method 1, the parameter β begins to increase at diameters of around 130 nm, whereas the onset for particles created via method 2 occurs at sizes of ~70 nm.

We modeled this effect by calculating the VDOS [19], assuming that each mode contributes a Lorentzian with a width $\Delta\nu$, for 10^5 particles with different particle diameters following a Gaussian distribution. We obtained the mean diameter and the standard deviation of this distribution from the SEM images of our samples. We assumed that ions in a nanocrystal with diameter d have a fast decay only if the VDOS of the nanocrystal at $\Delta = 35$ GHz is greater than 0. For each of the 10^5 particles, we simulated the fluorescence decay, either the sum of two exponential functions, in cases where fast decay is allowed, or only a single-exponential decay with radiative decay time in cases where fast decay is forbidden. We then averaged the individual decays to obtain the overall fluorescence decay for the ensemble of 10^5 particles. Finally, we fitted the resulting decay with Eq. (9), which returned the fraction of particles that suppress phonons β. The only free parameter in the simulations was the width $\Delta\nu$ of the individual vibrational modes, which we obtained through a fit to the experimental data. Note that the mode width was forced to be the same for all powders fabricated using a specific method. The results of the simulations are presented in Fig. 4.

For large crystal diameters d, the simulated values of β (for crystals created via either method) are around 0, which corresponds to the bulk value at 1.5 K. When we reduce d, the fraction of particles that suppress phonons starts to increase at two distinct diameters (130 nm for method 1 and 70 nm for method 2 crystals). This can be explained by different mode widths ($\Delta\nu = 1.2$ and 11 GHz for powders from methods 1 and 2, respectively) obtained from the simulations. If phonon modes are broad, as in powders from method 2, it is more likely that they overlap with the transition between the $^5\mathrm{D}_4\ a/b$ levels, even for small crystals. However, for sharp modes (powders from method 1), overlap becomes significant only for larger particles in which more modes exist. Note that the width of the phonon modes is related to the powder quality. In particular, crystallites with reduced surface roughness should feature narrower phonon modes. This leads us to conclude that powder 1 should be of higher quality, which, however, cannot be verified given the insufficient resolution of our SEM pictures. Note that the optical inhomogeneous line widths suggest that method 2 produces powders with less internal strain; however, it is not known whether there is a relationship between particle surface morphology and internal strain.

Overall, the simulated values are in good agreement with the experimental data for powders produced by either method, consistent with suppression of phonon-induced relaxation in sufficiently small powders. In particular, we observed the complete transition from large particles, where the relevant phonon processes are fully allowed, to the smallest particles, where we could not measure any contribution of the phonon-induced component to population relaxation.

In addition to a change in the amplitude of the fast nonradiative decay, we also expect a change in its characteristic decay time $T_{\mathrm{nr}} = 1/\gamma_{ba}$. For the fraction of particles with $\nu_{\min} \simeq \Delta_e$, the phonon density of states at Δ_e should deviate from the bulk value. With small enough particles we expect a decrease in the VDOS as the lowest phonon mode moves towards higher frequencies. Thus, because the rate of nonradiative relaxation is proportional to the VDOS, the phonon-induced decay rate for these nanocrystals should be slower than the one for the bulk, i.e., T_{nr} should increase with decreasing particle size. Note that in some cases, an enhanced VDOS can occur due to phonon confinement, which would lead to faster decay rates. Experimentally (see inset in Fig. 4), we observed a decrease in T_{nr} for some particles but we did not observe the expected increase due to a reduced density of states for the smallest particles. This is consistent with the conjecture of having sharp phonon modes (resulting from the fit of the decay ratios in Fig. 4), in which case the phonon cutoff occurs abruptly as the size is reduced so that the particles experience either a phonon rate equal to or larger than that in the bulk or no phonon decay. At this stage, the scatter of our experimental data unfortunately does not allow for a more in-depth analysis and interpretation.

IV. MEASUREMENT OF TEMPERATURE-DEPENDENT POPULATION RE-DISTRIBUTION

Another indication of the restriction of any nonradiative transition processes, including phonon modes, is the inhibition of thermalization (population re-distribution) between the two crystal-field levels $^5\mathrm{D}_4\, a/b$ after their initial population through decay from $^5\mathrm{D}_4\, f$. In the case of the bulk crystal, for $t > 1/\gamma_{ba}$, Eq. (3) gives the expected equilibrium population ratio, i.e., the Boltzmann distribution: $n_b^{\mathrm{bulk}}(t,T)/n_a^{\mathrm{bulk}}(t,T) = e^{\hbar\Delta/kT}$. In the extreme opposite case of total suppression of any nonradiative relaxation, the population ratio is constant and $n_b^{\mathrm{np}}(t)/n_a^{\mathrm{np}}(t) = 1$ if the initial populations are equal. In the case of our powder samples, where the suppression of phonons occurs only in a fraction of particles, we expect partial thermalization. From the expression of the total fluorescence intensity [see Eq. (9)], we can calculate the population ratio

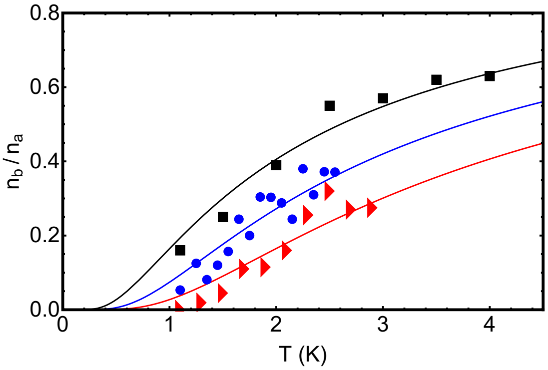

FIG. 5. Ratio of population n_b/n_a as a function of temperature in the bulk crystal (black squares) and in nanocrystals from method 1 of average diameter $d = 72$ nm (red triangles) and $d = 40$ nm (blue circles). Solid lines are best fits using Eq. (3), and shaded areas represent uncertainties.

$$\frac{n_b(t,T)}{n_a(t,T)} = \frac{(1-\beta)\, n_{\mathrm{bulk}}^b(t,T) + \beta\, n_{np}^b(T)}{(1-\beta)\, n_{\mathrm{bulk}}^a(t,T) + \beta\, n_{np}^a(T)}, \qquad (10)$$

where α is a coefficient accounting for an eventual difference in transition strength between the bulk and the powder samples, and β is the fraction of particles in which no thermalization (i.e., no fast nonradiative relaxation) occurs.

Experimentally, the population ratio $n_b(t,T)/n_a(t,T)$ can be extracted from the fluorescence decays for times $t > 1/\gamma_{ba}$. When there was no overlap between the transitions, i.e., in the case of the bulk crystal, we directly computed the ratio between the fluorescence intensities $i(t,T,f_{bj})/i(t,T,f_{aj})$ after background subtraction and averaged over all $t > 1/\gamma_{ba}$. We repeated this for $j = a, b$ and took the mean value. In the case of overlaps between neighboring transitions, i.e., in the case of small particles, we used Eqs. (5) and (8) and computed the population ratio for $t > 1\gamma_{ba}$ as follows:

$$\frac{n_b(t,T)}{n_a(t,T)} = \frac{I_{a\to j}(f_{aj})\, i(t,T,f_{bj}) - I_{a\to j}(f_{bj})\, i(t,T,f_{aj})}{I_{b\to j}(f_{bj})\, i(t,T,f_{aj}) - I_{b\to j}(f_{aj})\, i(t,T,f_{bj})}. \qquad (11)$$

Figure 5 shows the measured temperature dependence of n_b/n_a in the bulk crystal (black squares) and in nanocrystals from method 1 with an average diameter $d = 72$ nm (red triangles) and 40 nm (blue circles). We fitted the experimental points for each sample by Eq. (10). The only free parameters were the energy splitting Δ between the $^5\mathrm{D}_4$ a and b levels since the splitting might slightly change from powder to powder and the fraction β of particles in which no thermalization occurs between the levels $^5\mathrm{D}_4\, a/b$. We obtained $\Delta = 36 \pm 13$ GHz for the bulk, 72 ± 12 GHz for the 72-nm powder, and $\Delta = 42 \pm 11$ GHz for the 40-nm powder. In all cases the fits resulted in $\beta = 0$ with an uncertainty of ± 0.3 for the bulk, ± 0.1 for the 72-nm powder, and ± 0.14 for the 40-nm powder. Therefore, we observe no deviation from normal thermalization in the samples where the particles are small enough to inhibit phonon relaxation even though those samples did show a reduction of the nonradiative component in the fluorescence decays. This observation indicates that other processes, happening on time scales shorter than the 100-ns resolution of the detector used in our time-resolved fluorescence measurements, are responsible for the population re-distribution in our smallest nanocrystals. Such fast relaxation could be caused by coupling of the Tb^{3+} ions to tunneling modes characteristic of amorphous materials [30,31] (note that the increase in amorphous character as the particle size is reduced is supported by the observation of larger inhomogeneous broadening). Other explanations are relaxation driven by energy transfer [24] and interactions between ions and surface states.

V. CONCLUSION

In conclusion, we observed modifications in relaxation dynamics between crystal-field levels of $Tb^{3+}:Y_3Al_5O_{12}$ crystals as the particle size was varied from bulk to 40 nm and confirmed via absorption measurements that this effect is not due to local heating. One possible explanation is a modification of the VDOS in the nanocrystals, which restricts phonon processes between the first two crystal-field levels in the $^5D_4$ excited state manifold, which are separated by 35 GHz.

However, other measurements suggest a different explanation: population redistribution is still observed within the two closely spaced levels, meaning that other fast and nonradiative processes must enable this transition. These processes may arise from the partially amorphous character of the nanocrystals, even though significant effort was dedicated to achieving good crystal quality by exploring two synthesis methods and modifying different important parameters in each of them, such as the addition of surfactants or the annealing temperature. We note that the case of YAG is particularly difficult because of the high annealing temperature—which favors particle growth—required to crystallize the particles.

Improving the nanocrystal quality by optimizing fabrication methods, as well as switching to a different material with a lower annealing temperature, such as fluoride crystals, may enable one to observe the full phonon restriction. However, there may exist a fundamental limit to how small a particle can become while still preserving the spectroscopic properties of a large crystal; this limit is frequently estimated to be around 10 nm [32]. Our results suggest that, for YAG, it may be around 100 nm. Measurements of crystal structure may shine more light on this important question.

ACKNOWLEDGMENTS

The authors acknowledge the exceptionally detailed and in-depth review of our article and the referee's specific analysis and valuable suggestions. Furthermore, the authors acknowledge support from Alberta Innovates Technology Futures (ATIF), the National Engineering and Research Council of Canada (NSERC), the National Science Foundation of the USA (NSF) under Awards No. PHY-1415628 and No. CHE-1416454, and the Montana Research and Economic Development Initiative. W.T. was a Senior Fellow of the Canadian Institute for Advanced Research (CIFAR) and was, furthermore, supported through the Netherlands Organization for Scientific Research.

APPENDIX A: POWDER CHARACTERIZATION

For all investigations of population dynamics presented in the text, information about the morphology and size distribution of the various powders is needed to interpret the results. We obtained this information for powders from methods 1 and 2 using an SEM, with example images shown in Fig. 6. The images indicate that method 2 produces slightly less agglomerated powder compared to method 1. In addition, we confirmed that we obtained good single-phase crystalline YAG particles using powder XRD analysis. Figures 6(e) and 6(f) show the perfect overlap between the XRD spectrum of the $Tb^{3+}:Y_3Al_5O_{12}$ powders produced by methods 1 and 2 and the reference spectrum for YAG (JCPDS No. 30-0040). For selected powder samples, we also directly probed the quality of the crystal structure using a TEM, as shown in Fig. 6(d). The TEM analysis revealed that the crystallite orientations in agglomerated nanocrystals can remain nearly aligned throughout multiple grains when they are fused together. Since it is possible that phonon modes extend across several crystallites in these cases, we considered the effective particle size in agglomerated samples to be equal to the larger size of the approximately aligned agglomerations rather than the individual grain size. The effect of agglomeration on phonon propagation dynamics cannot be quantified at this stage.

In addition to using the TEM measurements, we investigated the degree to which the crystallites within the powder act as isolated particles versus being part of a larger agglomerated

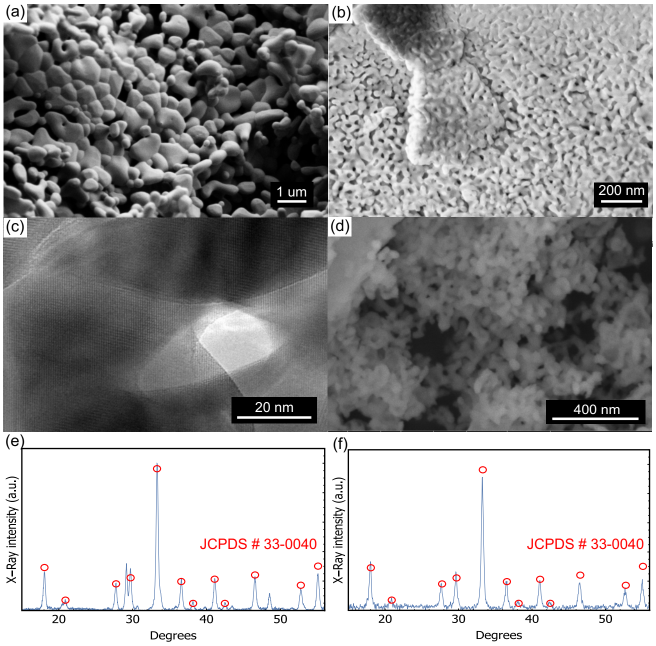

FIG. 6. Microscope images of 1% $Tb^{3+}:Y_3Al_5O_{12}$ created using method 1 and annealing at 1400 °C (a) or 900 °C (b, c) and using method 2 and annealing at 900 °C (d). (a, b, d) SEM images, showing the size distribution of the nanocrystals. (e, f) XRD spectra of powders produced by methods 1 and 2, respectively (solid blue lines), and the corresponding reference spectrum (JCPDS No. 30-0040; red circles) for YAG. (c) High-resolution TEM image showing the crystalline structure (narrow white lines), which can extend over several particles if they are agglomerated.

mass by observing the increase in radiative lifetime as the particle sizes are reduced. As known from relations such as the Strickler-Berg equation [33], the radiative lifetime T_{rad} of an electric dipole transition depends on the average index of refraction, n, of the material. Because of this, when the size of a fluorescing particle becomes comparable to the wavelength of the emitted light, the index of the medium surrounding the particle can have a significant effect on the radiative lifetime[20,34,35]. Consequently, we expect to observe an increase in the fluorescence lifetime as the average particle size in our powders is reduced. Note that strongly agglomerated particles would effectively act as a single, larger particle in this case.

We employ a simple analytical model to estimate the size dependence of the fluorescence lifetime for perfectly isolated particles. More precisely, we used the form of the Lorentz local field, sometimes referred to as the virtual cavity model [36], where the radiative lifetime in the medium T_{rad} is related to the lifetime in vacuum T_0 according to $1/T_{\mathrm{rad}} = (1/T_0)\, n_{\mathrm{eff}} (n_{\mathrm{eff}}^2 + 2)^2/9$, with n_{eff} being an effective index of refraction averaged over the surrounding medium within a distance of the order of the wavelength of light from the ion.

For particles smaller than the wavelength of light, the electric field extends beyond the particle. To evaluate n_{eff} for such particles, we assumed that the electric field of the emitted light experiences the bulk crystal dielectric constant within the particle and the vacuum dielectric constant outside the particle. We, furthermore, assumed that the electric field outside the particle decays as $E(r) = E_0 e^{-\frac{r}{l}}$ over the decay length l, which is equal to the evanescent field decay length outside of a bulk dielectric given by $l = \lambda_0/2\pi\sqrt{n^2 - 1}$ [37]. Here n is the refractive index of the bulk material and λ_0 the wavelength of the transition. The value of n_{eff} experienced by the emitting ion, and the resulting change in radiative lifetime, was then estimated by calculating the field-strength-weighted average dielectric constant over the area of nonzero electric field.

By using this simple model, we estimated the change in lifetime with particle size using only the known bulk crystal index, transition wavelength, and lifetime with no free parameters, resulting in the solid line in Fig. 7. We find that the measured lifetimes in our samples agree reasonably well with the calculated dependence (Fig. 7). With method 1, the radiative lifetime increases up to 7 ms, as the crystallite size decreases, but powders smaller than 50 nm show lifetimes similar to that of the bulk crystal, indicating that some degree of agglomeration is present. With method 2, the radiative lifetime increases up to 13 ms, indicating that the particles in powders synthesized with this method indeed behave as individual particles with sizes approximately equal to the values estimated from the SEM and TEM analysis.

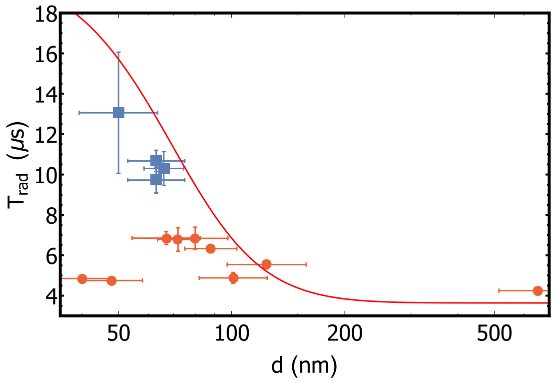

FIG. 7. Particle-size (d) dependence of the radiative lifetime of the ^{5}D$_4$ a level for powders from method 1 (red circles) and powders from method 2 (blue squares). The solid line shows the expected dependence.

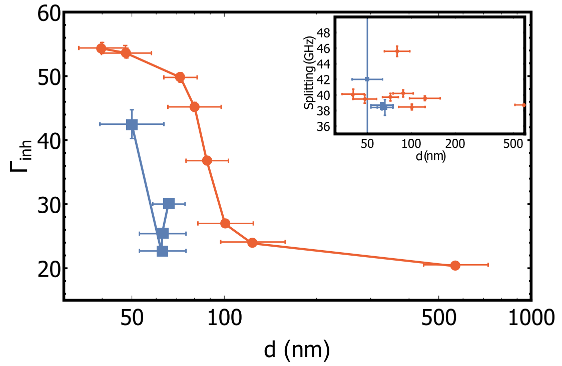

FIG. 8. Particle-size dependence of the inhomogeneous line width for powders from method 1 (red circles) and powders from method 2 (blue squares). Inset: Splitting Δ between the ^{5}D$_4$ a/b levels versus particle size. Solid lines are guides for the eye.

APPENDIX B: SPECTROSCOPIC INVESTIGATIONS OF POWDER QUALITY

To ensure that we can selectively collect fluorescence from the two excited levels ^{5}D$_4$ a/b for each of our samples, we recorded fluorescence spectra by scanning the monochromator over the four lines connecting ^{5}D$_4$ $a/b \rightarrow$ ^{7}F$_5$ a/b. As shown in Fig. 8, we observed that with both fabrication methods, the smallest nanocrystals feature an increased inhomogeneous broadening compared to the bulk. This increase, which was expected due to the increased amount of strain, was not observable in the XRD spectra due to the limited resolution of our XRD diffractometer (Rigaku Multiflex). The observation of increased inhomogeneous broadening is consistent with the emergence of relaxation that is facilitated by amorphous phases and surface defects (see the text). However, as shown in the inset in Fig. 8, the splitting Δ between the ^{5}D$_4$ a/b levels does not change with particle size, which indicates that the ions' crystal-field splittings and local lattice symmetry are not measurably different in the small powders.

APPENDIX C: LOCAL TEMPERATURE MEASUREMENT

In past measurements, the thermal conductivity of small powders in a gas environment was observed to decrease with particle size due to two effects. First, the phonon scattering length is reduced in small powders, and second, heat flow is hindered by the surface resistance of the small particles contained in the powder [38–40]. These effects could lead to a locally elevated powder temperature, especially when the powder is probed using a high-power laser. An elevated sample

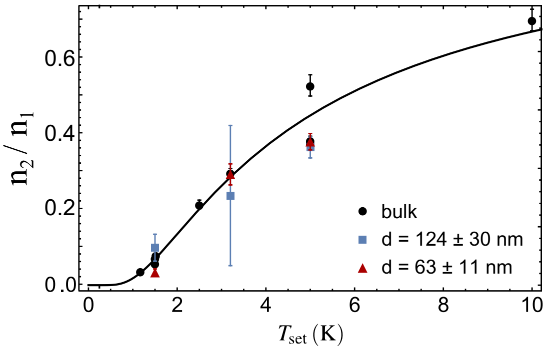

FIG. 9. Ratio n_2/n_1 of populations in the ground manifold ^{7}F$_6$ b/a levels as a function of the temperature $T_{\rm set}$ read by the cryostat sensor for a bulk crystal (black circles) and nanocrystalline powder samples with diameters $d = 124 \pm 30$ nm, produced by method 1 (blue squares), and $d = 63 \pm 11$ nm, produced by method 2 (red triangles). The solid line is the fit to a Boltzmann distribution with $\Delta_g = 83.5$ GHz. Note that the large error bar for 3.2 K and $d = 124$ nm is caused by the large uncertainty of the fit to that particular absorption spectrum.

temperature in turn would produce significant changes in population relaxation and thermalization that could potentially be misinterpreted as arising from other effects. To ensure that the laser excitation did not induce localized heating, a direct temperature measurement that enables the true internal temperature of the particles to be monitored is required.

We measured the internal temperature for each sample by recording the absorption spectrum ^{7}F$_6\,a, b \rightarrow {}^5D_4\,f$ and comparing the populations n_1 and n_2 on the first and second crystal-field levels ^{7}F$_6\,a$ and b of the ground-state multiplet, which are separated by $\Delta_g = 83$ GHz. This allowed us to determine the effective internal sample temperature T via the Boltzmann law $n_2/n_1 = A\exp\{-\Delta_g/k_BT\}$, with k_B the Boltzmann constant. We obtained the coefficient A, which depends on the relative oscillator strengths of the transitions, from a calibration measurement using a 1% Tb:YAG bulk crystal, which we assumed to thermalize quickly to the temperature $T_{\rm set}$ that was measured by the cryostat sensor. The temperature-dependent population ratio n_2/n_1 is shown in Fig. 9 for a selected set of nanocrystals. The close overlap between the bulk and the powder results confirms that all powders thermalize as well as the bulk when immersed in liquid helium or vapor and that the laser is not measurably heating the nanocrystals, even for the smallest sizes. Since these measurements are conducted using the same laser power and focusing parameters as those used for all other measurements described in the text, they confirm that the changes in dynamics that we observe in the powders are not caused by local heating. Also, with this method, we ensure that the ions that are studied in the relaxation dynamics measurements (as in the text) are also the same ions that are used to measure the temperature.

---

[1] H. de Riedmatten and M. Afzelius, *Quantum Light Storage in Solid State Atomic Ensembles* (Springer International, Cham, Switzerland, 2015), pp. 241–273.

[2] K. Heshami, D. G. England, P. C. Humphreys, P. J. Bustard, V. M. Acosta, J. Nunn, and B. J. Sussman, J. Mod. Opt. **63**, 2005 (2016).

[3] A. Sipahigil, R. E. Evans, D. D. Sukachev, M. J. Burek, J. Borregaard, M. K. Bhaskar, C. T. Nguyen, J. L. Pacheco, H. A. Atikian, C. Meuwly, R. M. Camacho, F. Jelezko, E. Bielejec, H. Park, M. Lončar, and M. D. Lukin, Science **354**, 847 (2016).

[4] B. Hensen, H. Bernien, A. E. Dreau, A. Reiserer, N. Kalb, M. S. Blok, J. Ruitenberg, R. F. L. Vermeulen, R. N. Schouten, C. Abellan, W. Amaya, V. Pruneri, M. W. Mitchell, M. Markham, D. J. Twitchen, D. Elkouss, S. Wehner, T. H. Taminiau, and R. Hanson, Nature **526**, 682 (2015).

[5] M. P. Hedges, J. J. Longdell, Y. Li, and M. J. Sellars, Nature **465**, 1052 (2010).

[6] E. Saglamyurek, N. Sinclair, J. Jin, J. A. Slater, D. Oblak, F. Bussières, M. George, R. Ricken, W. Sohler, and W. Tittel, Nature **469**, 512 (2011).

[7] P. C. Maurer, G. Kucsko, C. Latta, L. Jiang, N. Y. Yao, S. D. Bennett, F. Pastawski, D. Hunger, N. Chisholm, M. Markham, D. J. Twitchen, J. I. Cirac, and M. D. Lukin, Science **336**, 1283 (2012).

[8] S. Hong, M. S. Grinolds, L. M. Pham, D. Le Sage, L. Luan, R. L. Walsworth, and A. Yacoby, MRS Bull. **38**, 155 (2013).

[9] R. C. Powell, *Physics of Solid-State Laser Materials* (Springer-Verlag, New York, 1998).

[10] A. J. Kenyon, Prog. Quantum Electron. **26**, 225 (2002).

[11] T. Jüstel, H. Nikol, and C. Ronda, Angew. Chem. Int. Ed. **37**, 3084 (1998).

[12] F. Wang, Y. Han, C. S. Lim, Y. Lu, J. Wang, J. Xu, H. Chen, C. Zhang, M. Hong, and X. Liu, Nature **463**, 1061 (2010).

[13] E. Downing, L. Hesselink, J. Ralston, and R. Macfarlane, Science **273**, 1185 (1996).

[14] X. L. Ruan and M. Kaviany, Phys. Rev. B **73**, 155422 (2006).

[15] T. Lutz, L. Veissier, C. W. Thiel, P. J. T. Woodburn, R. L. Cone, P. E. Barclay, and W. Tittel, Sci. Technol. Adv. Mater. **17**, 63 (2016).

[16] T. Lutz, L. Veissier, C. W. Thiel, P. J. Woodburn, R. L. Cone, P. E. Barclay, and W. Tittel, J. Lumines. **191**, 2 (2017).

[17] T. Zhong, J. M. Kindem, E. Miyazono, and A. Faraon, Nat. Commun. **6**, 8206 (2015).

[18] A. Ferrier, C. W. Thiel, B. Tumino, M. O. Ramirez, L. E. Bausá, R. L. Cone, A. Ikesue, and P. Goldner, Phys. Rev. B **87**, 041102 (2013).

[19] T. Lutz, L. Veissier, C. W. Thiel, R. L. Cone, P. E. Barclay, and W. Tittel, Phys. Rev. A **94**, 013801 (2016).

[20] H.-S. Yang, S. P. Feofilov, D. K. Williams, J. C. Milora, B. M. Tissue, R. S. Meltzer, and W. M. Dennis, Physica B: Condens. Matter **263**, 476 (1999).

[21] H.-S. Yang, K. Hong, S. Feofilov, B. M. Tissue, R. Meltzer, and W. Dennis, J. Lumines. **83**, 139 (1999).

[22] G. K. Liu, H. Z. Zhuang, and X. Y. Chen, Nano Lett. **2**, 535 (2002).

[23] B. Mercier, C. Dujardin, G. Ledoux, C. Louis, O. Tillement, and P. Perriat, J. Lumines. **119**, 224 (2006).

[24] T. Förster, Ann. Phys. **437**, 55 (1948).

[25] L. Mezeix and D. J. Green, Int. J. Appl. Ceram. Technol. **3**, 166 (2006).

[26] N. Kaithwas, M. Dave, S. Kar, S. Verma, and K. S. Bartwal, Cryst. Res. Technol. **45**, 1179 (2010).

[27] H. Gong, D.-Y. Tang, H. Huang, and J. Ma, J. Am. Ceram. Soc. **92**, 812 (2009).

[28] T. W. Hänsch, Appl. Opt. **11**, 895 (1972).

[29] H. Lamb, Proc. Lond. Math. Soc. **s1-13**, 189 (1881).

[30] P. W. Anderson, B. I. Halperin, and C. M. Varma, Philos. Mag. **25**, 1 (1972).

[31] W. A. Phillips, J. Low Temp. Phys. **7**, 351 (1972).

[32] X. C. G. Liu, *Handbook on the Physics and Chemistry of Rare Earths* (Elsevier Science & Technology, Amsterdam, 2007).

[33] S. J. Strickler and R. A. Berg, J. Chem. Phys. **37**, 814 (1962).

[34] H. Schniepp and V. Sandoghdar, Phys. Rev. Lett. **89**, 257403 (2002).

[35] A. Aubret, A. Pillonnet, J. Houel, C. Dujardin, and F. Kulzer, Nanoscale **8**, 2317 (2016).

[36] S. Scheel, L. Knöll, and D.-G. Welsch, Phys. Rev. A **60**, 4094 (1999).

[37] F. de Fornel, *Evanescent Waves* (Springer-Verlag, Berlin, 2001).

[38] K. W. Garrett and H. M. Rosenberg, J. Phys. D **7**, 1247 (1974).

[39] T. Rettelbach, J. Säuberlich, S. Korder, and J. Fricke, J. Non-Cryst. Solids **186**, 278 (1995).

[40] D. E. Brodie and C. F. Mate, Can. J. Phys. **43**, 2344 (1965).